Monolithic Biohybrid Flexure Mechanism Actuated by Bioengineered Skeletal Muscle Tissue

Andrea Bartolucci, Judith Fuentes, Daniele Guarnera, Florencia Lezcano, Maria Crespo-Cuadrado, Lorena Guachi-Guachi, Francesco Iacoponi, Carlotta Salvatori, Riccardo Collu, Massimo Barbaro, Stefano Lai, Leonardo Ricotti, Samuel Sánchez, and Lorenzo Vannozzi**

Skeletal muscle tissue represents an attractive powering component for biohybrid robots, as traditional actuators used in the soft robotic context often rely on complex mechanisms and lack scalability at small dimensions. This article proposes a monolithic biohybrid flexure mechanism actuated by a bioengineered skeletal muscle tissue. The design leverages the contractile properties of a bioengineered skeletal muscle to produce a bending motion in a monolithic, tubular mechanism made of a soft and biocompatible silicone blend. This structure integrates two cylindrical pillars that facilitate force transmission from the bioengineered muscle tissue. Performance assessments reveal excellent contractile and stable behavior upon electrical stimulation, compared to current biohybrid actuation systems, with enhanced performance as the mechanism's internal and external diameters decrease. Finite-element simulations further reveal distinct force–displacement responses in mechanisms with different flexural rigidity. This innovative, scalable, and easy-to-fabricate design represents a significant step forward in the development of novel biohybrid machines.

1. Introduction

Biohybrid soft robotics is a rapidly growing research area that combines the unique capabilities of living cells with the properties of artificial components, with the potential to create the next generation of soft robots.[1] Traditional actuators, such as pneumatics, hydraulics, shape-memory alloys, and dielectric elastomers, face significant challenges in achieving the same level of fluidity and adaptability found in biological systems. These systems, driven by external power sources like air pressure, electrical fields, or heat, often suffer from relatively low efficiency, high variability of their performance at different scales, and lack of self-healing capabilities.[2] In contrast, muscle tissue has garnered significant attention as an ideal bioactuation mechanism due to its intrinsic features, such as controllable contractile behavior, high-energy efficiency, performance invariance at different scales, and self-healing ability.[3,4]

Integrating muscle tissues into artificial systems aims to replicate the soft, flexible, and lifelike movements that are challenging for conventional robotic actuators.[5] Biohybrid actuators rely on the contraction and relaxation of muscle cells, stimulated either electrically, chemically, or optogenetically.[6,7]

In recent years, skeletal and cardiac muscle–based biohybrid actuators have been utilized in various designs. These include

A. Bartolucci, D. Guarnera, L. Guachi-Guachi, F. Iacoponi, C. Salvatori, L. Ricotti, L. Vannozzi
The BioRobotics Institute
Scuola Superiore Sant'Anna
56127 Pisa, Italy
E-mail: leonardo.ricotti@santannapisa.it; lorenzo.vannozzi@santannapisa.it

A. Bartolucci, D. Guarnera, L. Guachi-Guachi, F. Iacoponi, C. Salvatori, L. Ricotti, L. Vannozzi
Department of Excellence in Robotics and AI
Scuola Superiore Sant'Anna
56127 Pisa, Italy

The ORCID identification number(s) for the author(s) of this article can be found under https://doi.org/10.1002/aisy.202400989.

DOI: 10.1002/aisy.202400989

J. Fuentes, F. Lezcano, M. Crespo-Cuadrado, S. Sánchez
Institute for Bioengineering of Catalonia (IBEC)
The Barcelona Institute for Science and Technology (BIST)
Barcelona 08028, Spain

S. Sánchez
Institució Catalana de Recerca i Estudis Avancats (ICREA)
Barcelona 08010, Spain

R. Collu, M. Barbaro, S. Lai
Department of Electrical and Electronic Engineering
University of Cagliari
Piazza D'Armi, 09123 Cagliari, Italy

planar geometries, single-cell layers, also termed thin films,[8,9] hydrogel-based 3D constructs,[10,11] or bio-bots.[12–14] Skeletal muscle cells, in particular, represent a promising actuation module, due to their precise control over contraction, unlike cardiac muscle, which contracts spontaneously. Engineered skeletal muscle tissues have been widely used in biohybrid robotics to generate biomimetic movements, such as grasping,[15] pumping,[16] crawling,[17,18] swimming,[19] rotating joints for carrying objects,[20] and walking.[21]

However, many existing skeletal muscle–powered actuators are limited to linear movements.[14,19] For example, biohybrid walkers use muscle contractions to deform a polymeric substrate, generating crawling motion.[17,18] Current biohybrid actuation approaches, based on rotational or traditional linear actuators, may not fully capture the subtleties of natural movements.

Flexure movements may play a crucial role in biohybrid soft robotics, as they can closely mimic the flexible, adaptable, and lifelike motions found in biological systems. These mechanisms rely on the elasticity of materials to provide motion in mechanisms. Flexural systems can be deformed with an infinite-motion resolution, minimizing the drawbacks of traditional joints, such as friction, wear, lubrication, and backlashes, by playing with a monolithic design.[22] The versatility of flexure mechanisms has contributed to significant breakthroughs in different fields, ranging from robotics to micromachining and microfabrication.[23] Flexure-based systems are inherently biomimetic and may assist in replicating the bending of limbs, the flexion of tendons, or the curvature of plant stems.[24] Incorporating flexure mechanisms into biohybrid robots would allow sophisticated bending and curving actions, enabling these systems to adapt their shape and motion for fine-tuned interactions with complex and dynamic environments.[25]

Despite recent advancements, flexure actuation architectures within biohybrid systems are under-explored. Here, the design parameters of the robotic structure assume a crucial role, as well as the need to move to softer materials to maximize the motion of biohybrid actuators.[26,27] Current materials are often limited by the rigidity of structures like parylene, or polydimethylsiloxane (PDMS) in its conventional monomer/curing agent ratio.[28–30] To fully exploit the capabilities of biohybrid actuation, careful attention must be paid to the softness and elasticity of the supporting material, crucial for leveraging the contractile properties of engineered muscle tissue to promote soft, flexural movements in biohybrid robots.[31] Furthermore, biological muscle actuation offers the potential for miniaturization, opening doors to the development of microscale biohybrid robots. Miniaturization is essential in biohybrid robotics because it permits more precise interactions with biological systems, improves efficiency (since the main problem of scaling up tissues is the lack of viability/functionality), and enables integration into delicate/complex environments (e.g., the vascular system or other body channels and cavities).

This work introduces a biohybrid flexure mechanism (BFM) driven by the contractile action of a bioengineered skeletal muscle tissue. The BFM is fabricated by molding using a soft and biocompatible silicone blend and is based on two cylindrical pillars integrated into the outer surface to let the muscle transfer its contraction force to the structure. Two configurations with decreasing internal diameter (2 and 0.7 mm) are evaluated to explore the role of flexural rigidity in the flexural behavior of the BMF upon muscle bioactuator contraction. Finite-element (FE) simulations are implemented to identify the force needed by the muscle construct to bend the flexure mechanisms at different scales. The proposed mechanism offers a promising alternative to existing skeletal muscle–powered actuation strategies, relying on a scalable, monolithic tubular structure composed of a novel and biocompatible soft silicone blend. This approach combines the contractile potential of in vitro engineered skeletal muscle tissue with the precision and versatility of soft material prototyping. Furthermore, this work demonstrates that the BFM configuration can be adapted for specific functionalities in biohybrid systems, such as targeted substance delivery or the gripping of small objects.

2. Results and Discussion

2.1. Characterization of the 3D Bioengineered Skeletal Muscle Bioactuator

The skeletal muscle tissue employed in this work was produced via mold casting. Fabrication of muscle bioactuators using circular-shaped molds have demonstrated, in previous studies, high scalability and easy integration into different flexible structures, such as serpentine-like skeletons or posts.[19,32] **Figure 1**a shows a scheme of the fabrication and integration of the bioengineered muscle within the BFM. In this process, a bioink containing C2C12 myoblasts encapsulated in a Matrigel/fibrinogen-based matrix was cast in a 3D-printed PDMS-based circular mold. After 2 days in growth medium (GM), during which myoblasts proliferated within the 3D matrix, the muscle ring was transferred to a PDMS-based two-post system and maintained in a differentiation medium (DM) until complete myotube formation, which required 7 days. After tissue maturation, the biofabricated muscle bioactuator was assembled into the flexure system, which also contained posts ensuring tissue integration. Finally, the performance of the resulting BFM, powered by the contraction of the muscle tissue, was evaluated under electrical pulse stimulation (EPS). A comparison between in vitro and in silico analyses was done, to evaluate the mechanical response of the BFM under muscle contraction. This allowed the resulting deformation of the flexure structure to be revealed, as well as the force needed to bend the flexure mechanism at different scales. In this workflow, the use of the PDMS-based post system was essential for the proper maturation of the muscle tissue, as it provided tension during the myoblast differentiation into myocytes and their further fusion into fully mature multinucleated myotubes (Figure 1b). According to previously published protocols, we set the distance between the two posts from their centers at 9 mm, which supported the differentiation of skeletal muscle cells and enabled performance evaluation of the tissues.[10,19,33,34]

To evaluate the contractile behavior of the bioengineered skeletal muscle rings, an indicator of tissue maturation, contraction force was assessed on day 7 of differentiation under EPS applying 1 and 30 Hz to measure the twitch and tetanic contractions of the muscle tissues, respectively (Figure 1c). This analysis was performed using the two-post system, initially adopted to culture the muscle tissue and now used as a force measurement platform (further details are provided in Experimental Section).

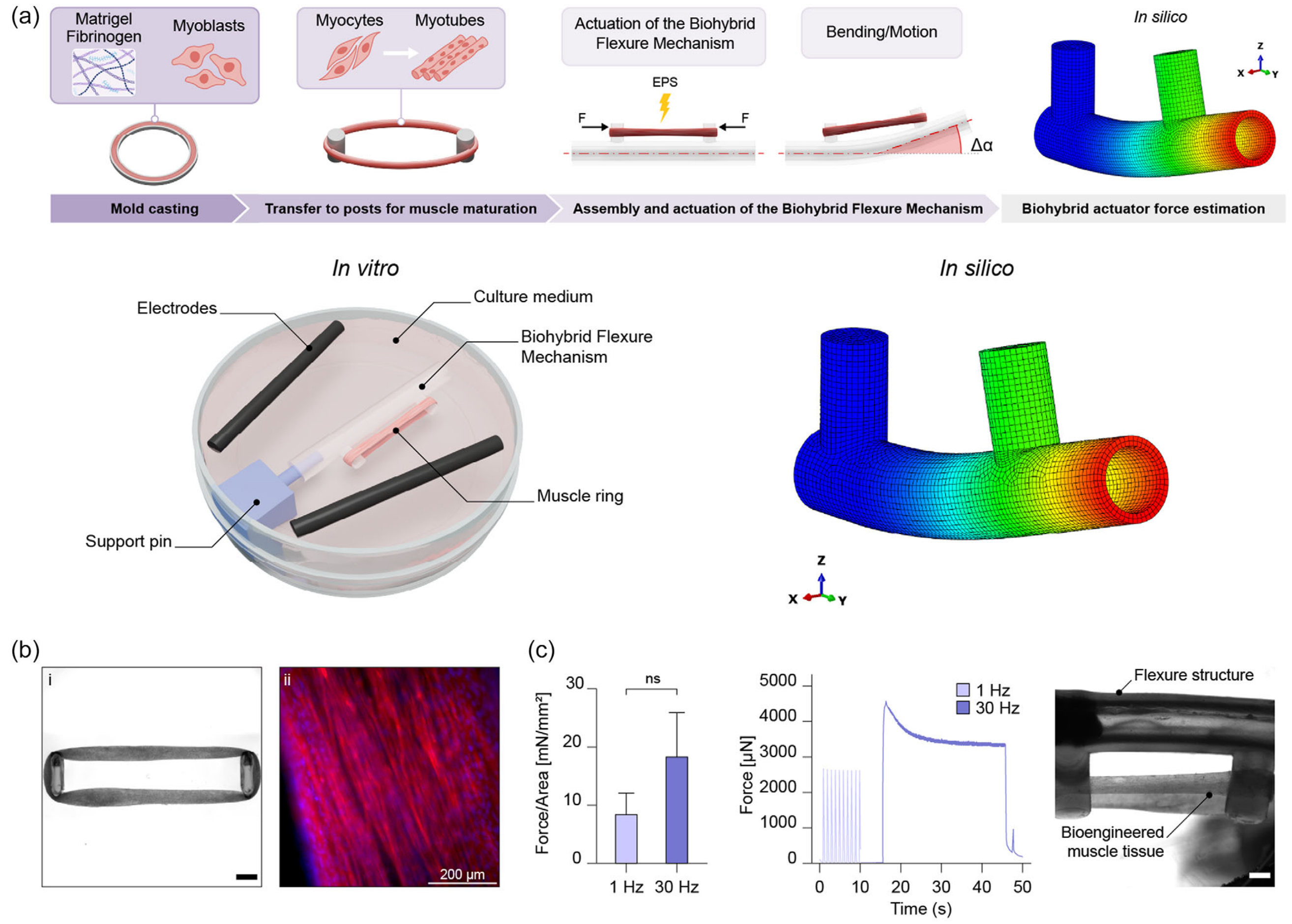

Figure 1. Overview of the fabrication and integration of the bioengineered muscle within the biohybrid flexure mechanism and contraction force evaluation. a) Artistic illustration of the study workflow: first, the 3D skeletal muscle–based bioactuator was fabricated by mold casting and then transferred to a two-post system during the muscle differentiation process to form aligned and multinucleated myotubes. Once assembled in the biohybrid flexure mechanism, it was actuated under electrical pulse stimulation (EPS) and the performance (bending/motion) was evaluated through bright-field microscopy. Finally, an in vitro–in silico comparison was performed to elucidate the force needed by the muscle construct to bend the flexure mechanisms at different scales. b) Bright-field image of the muscle bioactuator in the two-post system (scale bar: 1 mm), and immunofluorescence staining of actin (phalloidin) and nucleus (Hoechst) of the differentiated multinucleated myotubes. Scale bar: 200 µm. c) Left: graph of contraction force normalized with tissue cross-sectional area (force/area in mN mm^{-2}) generated by muscle bioactuators under EPS applying a frequency of 1 Hz and 30 Hz. Wilcoxon test was used to assess statistical significance (p value < 0.05, $N = 3$). Values are reported as mean and standard deviation. Right: graph shows an example of the contraction patterns (twitch and tetanus) obtained when applying 1 and 30 Hz. d) Bright-field image of the muscle bioactuator assembled in the biohybrid flexure mechanism. Scale bar: 1 mm.

When applying 1 Hz frequency, muscle tissues exerted an average force of 2.1 mN, which resulted in a stress of $8.3 \pm 3.7\ \text{mN mm}^{-2}$. Significantly higher stresses of $18.3 \pm 7.6\ \text{mN mm}^{-2}$ (average force: 3.7 mN) were obtained during tetanic contractions induced by 30 Hz stimulation. Electrical stimulation was applied using a biphasic asymmetric waveform, which alternates polarity to prevent charge buildup at the electrodes and within the tissue. Such a charge balance reduced the risk of tissue damage and provided a more physiological stimulus, enhancing calcium flux and contractile response.[35–37] The high variability in the force values observed may derive from biological differences between muscle tissues. Indeed, although mold casting is a straightforward and accessible method for tissue biofabrication, its lack of automation can introduce significant variability among the tissue constructs.

After confirming that the muscle tissue rings exhibited contractility at 1 Hz (twitch contractions) and 30 Hz (tetanic contractions), they were integrated into the BFM. The shape of the muscle rings allowed ease of anchoring around the pillars of the flexure system, as shown in Figure 1d.

2.2. Material Selection for the BFM: Mechanical and Biological Analyses

PDMS and EcoFlex are widely used silicone materials, which are particularly interesting for fabricating biomedical devices due to their biocompatibility, flexibility, and compatibility with the molding process.[38,39] Sylgard 184 is a PDMS-based silicone extensively studied by the microfluidics community due to its advantageous features, such as biocompatibility, optical clarity, processability, moldability, and moderate tear resistance, which have facilitated the construction of various demonstrators.[40] While Sylgard 184 establishes the standard for commercial silicones, it exhibits restricted extensibility (up to 135% for softer formulations), low tear resistance, and a comparatively elevated Young's modulus typical of most commercial silicone elastomer compositions.[40,41] In contrast, EcoFlex is easy to manufacture and has a high tear strength and a smaller elastic modulus. The mechanical analysis was conducted in the first instance on PDMS at varying monomer/reticulant agent ratios (10:1 and 20:1), and EcoFlex, by assessing the Young's modulus from the initial 10% of the materials' stress–strain curves (**Figure 2**a). The graph indicates that the PDMS 10:1 stiffness is significantly higher than the other data (mean value: 1.13 MPa). As the concentration of the curing agent diminishes, the Young's modulus markedly declines. EcoFlex is distinguished by a relatively low Young's modulus, with a mean value of 0.05 MPa.[41] Then, we started evaluating blends between PDMS and EcoFlex with the purpose of identifying a softer and more moldable (i.e., higher tear strength) but still yet biocompatible blend than PDMS 20:1 (mean value: 0.34 MPa) that would constitute the material for the fabrication of the BFM. This analysis started by first analyzing blend ratios of 1:1 and 1:2 of PDMS-EcoFlex, utilizing PDMS 10:1 and 20:1 with EcoFlex. Results indicated that adding EcoFlex to PDMS up to the ratio 1:2 did not soften the blend, as Young's modulus did not decrease. Subsequently, we opted to eliminate the curing agent from one of the silicone constituents, such as PDMS, to further reduce

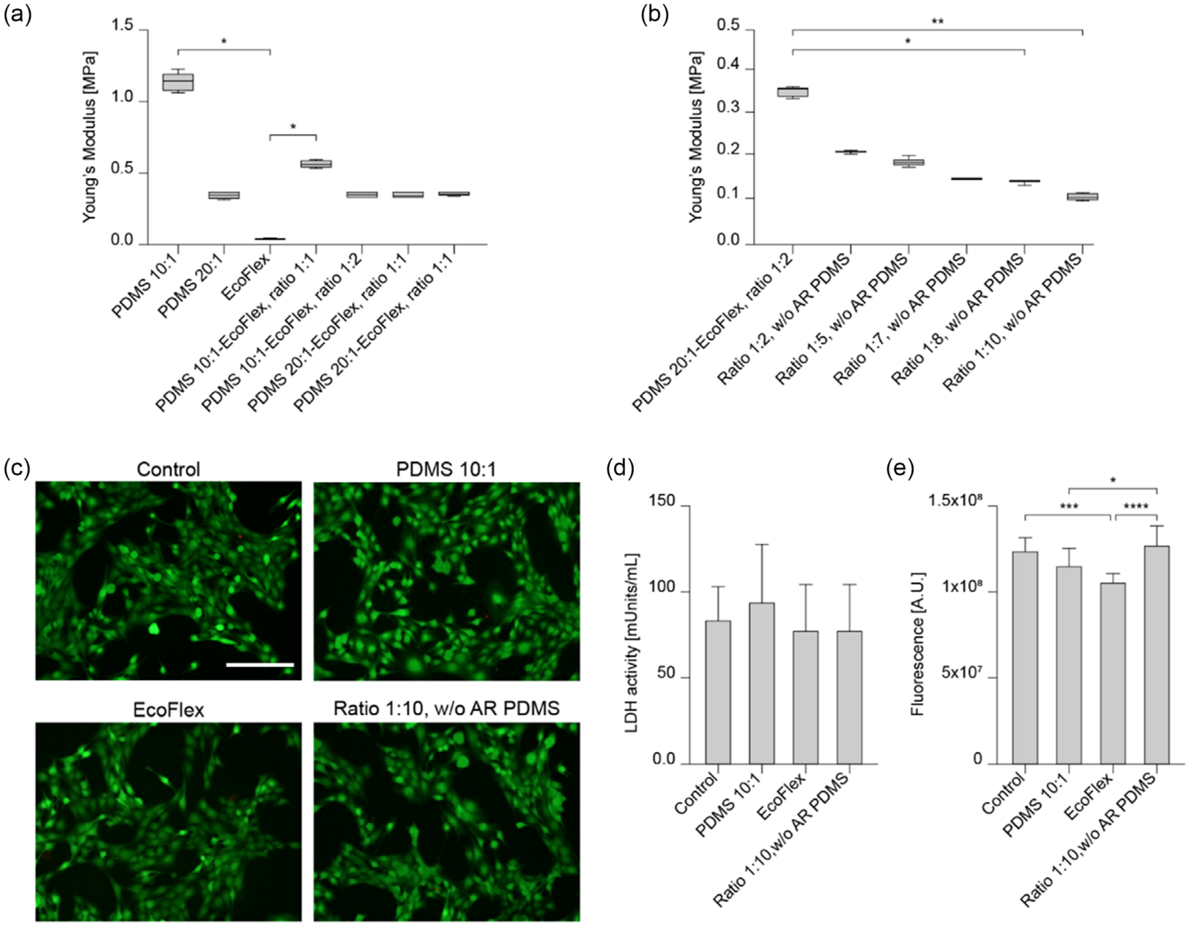

Figure 2. Characterization of silicone compositions for biohybrid flexure mechanism fabrication. a) Young's moduli of different material formulations (PDMS 10:1, 20:1, and EcoFlex) and different blends (ratio 1:1 and 1:2). Data are reported with boxes and whiskers. $N = 4$. Kruskal–Wallis test was performed to compare data values. b) Comparison of the Young's modulus of different PDMS/EcoFlex blends varying the EcoFlex content ratio from 1:2 to 1:10 and removing the reticulant agent (AR) of PDMS (w/o AR PDMS). Data are reported with boxes and whiskers. $N = 4$. The Kruskal–Wallis test was performed to compare data values. c) Representative Live/Dead images of C2C12 muscle cells (green: viable cells; red: dead cells; scale bar: 200 μm) of the Control, PDMS 10:1, EcoFlex, and mixing between 10 parts of EcoFlex and 1 part of PDMS (Ratio 1:10, w/o AR PDMS). d) Detection of the lactase dehydrogenase (LDH) activity of C2C12 muscle cells analyzed for each sample type. $N = 6$. Data are reported with a bar plot showing the mean and standard deviation. Analysis of variance (ANOVA) with Tukey's post hoc test analysis was performed to compare data values. e) C2C12 cell metabolism, reported in terms of fluorescence signal read at 560 nm (A.U.). $N = 6$. Data are reported with a bar plot showing the mean and standard deviation. ANOVA with Tukey's post hoc test analysis was performed to compare data values. $* = p$ value < 0.05, $**p$ value $= 0.01$, $*** = p$ value < 0.001, and $**** = p$ value < 0.0001.

the Young's modulus of the blend. We hypothesized that the curing agent of PDMS and EcoFlex, being both tin-based catalysts, may compete, thereby compensating for the softening effect caused by the combination of a softer component (e.g., EcoFlex) with a more rigid one (e.g., PDMS). Figure 2b demonstrates that the exclusion of the curing agent from PDMS induced a reduction in the Young's modulus of the PDMS-EcoFlex blends at an increasing ratio, that was significant at 1:8 (p value < 0.05) and 1:10 (p value < 0.01). We identified a material formulation that resulted in a noticeable decrease from 1.13 (PDMS 10:1) to 0.11 MPa (PDMS-EcoFlex ratio 1:10, without the reticulant agent of PDMS). Such a reduction is crucial to maximize the performance of the BFM, as the Young's modulus is inversely proportional to the displacement.[14,27]

Then, we proceeded with the evaluation of the blend cytotoxicity, by exposing C2C12 cell monolayers for 72 h to cell culture media that was previously conditioned by the incubation with different silicone formulations. As previously mentioned, Sylgard 184 displays advantageous features such as biocompatibility. The addition of a considerable portion of EcoFlex, which is less adopted in cell-compatible environments, could cause potentially harmful effects on muscle cells.[42] The LDH assay was used to evaluate cytotoxicity and cell membrane integrity loss, while the PrestoBlue assay was used to assess cell metabolic activity. Such tests revealed high cell viability, with no observable variations in cell morphology, as illustrated in Figure 2c. The examination of lactate dehydrogenase (LDH) release revealed no significant differences in LDH levels across the various materials (Figure 2d). This result indicated that the cells were viable and that the material under investigation did not cause damage to the cell membrane compared to the control. In contrast, cell metabolic activity resulting from cell-EcoFlex interaction significantly differed from that of the control (Figure 2e). Interestingly, the chosen mixture (Mixing ratio EcoFlex-PDMS 10:1, excluding PDMS reticulant agent) exhibited no metabolic distinction from the control. This outcome highlighted the absence of detrimental effects associated with the inclusion of EcoFlex in the chosen material blend, suggesting that even a minor inclusion of PDMS was crucial for attaining superior biological characteristics compared to the exclusive use of EcoFlex.

2.3. Assembly and Evaluation of the BFM at Different Scales

Mold casting was chosen for the fabrication of the BFM as it enables the fabrication of complex shapes, channels, and other features with high precision and consistency.[43] Smooth mold components were fabricated through stereolithography, which assured a high resolution, thus preventing the presence of roughness on the final prototype surface. An example of the components used to assemble the BFM is reported in Figure S1a, Supporting Information.

Two monolithic designs for the BFM were investigated, based on a tubular structure with a length of 15 mm and a wall thickness of 0.3 mm, with internal diameters of 2 and 0.7 mm (Figure S1b,c, Supporting Information). These designs were referred to as BFM A (BFM-A) and BFM B (BFM-B), respectively (**Figure 3**a). Two pillars were included at the outer side of the flexure mechanism at a distance of 9 mm between their centers, to constitute the anchors from which the bioactuator can transfer the force exerted upon contraction, according to the results found in Section 2.1. For the BFM-A, pillars were shaped with a diameter of 2 mm, and a height of 3 mm (Figure 3b), while in the case of the BFM-B, the pillars were scaled down while keeping the ratio equal to 2/3 while scaling the size (diameter: 1 mm; height: 1.5 mm) (Figure 3c). The mechanism was modeled as a hollow tube to reduce its buckling resistance due to the reduced moment of inertia and thin-walled structure. Thus, we investigated the influence of the flexure mechanism size on the bending angle and vertical displacement obtained upon muscle contraction by maintaining the pillars' distance and decreasing the internal and external diameters. In both cases, a portion of the distal side was left without any elements to evaluate the vertical displacement and bending angle of the BFM, whereas the first pillar remained fixed by means of a support pin (Figure 1a).

The bioactuator was actuated by imposing different EPS protocols, which differed for the applied electrical fields (0.33, 0.66, and 1 V mm^{-1}) and different pulse widths (2, 4, and 10 ms), at a frequency that led to the tetanus phenomenon (i.e., 30 Hz). Indeed, stimulation at frequencies that cause tetanus facilitated the achievement of higher contraction force,[20] which positively contributed to the maximization of the performance of the BFM, as also shown in Section 2.1. At the same time, the maximum electric field was kept at 1 V mm^{-1}.[20,28]

Movie S1 and S2, Supporting Information show the different deflection achieved in the BFM-A and BFM-B upon the application of electrical stimulation at 1 V mm^{-1}. Videos also show that in both cases, the BFM recovered its position upon bending without permanent deformation or tearing. A representative example of the vertical displacement overtime achieved by the two mechanisms is reported in Figure 3d.

More in detail, results showed that by increasing the electric field, the BFM-A increased the bending angle from $7.80° \pm 2.82°$ to $10.83° \pm 1.26°$ (Figure 3e). Conversely, the vertical displacement experienced by such a mechanism improved from an average value of 1.52 ± 0.50 to 2.10 ± 0.24 mm (Figure S2, Supporting Information). In contrast, for the BFM-B, the maximum bending angle was found at $19.23° \pm 3.26°$ (Figure 3e), whereas the maximum displacement was found at 3.31 ± 0.95 mm (Figure S2, Supporting Information) when applying a stimulation of 1 V mm^{-1}.

Results indicated that the decrement of the diameters led to a significant increase in the angle achieved upon contraction, thus in the vertical displacement of the BFM. For instance, the BFM-B stimulated at the highest electric field (1 V mm^{-1}) has doubled the bending angle and the vertical displacement found in the BFM-A with the bioactuator stimulated at the lowest electric field (0.33 V mm^{-1}). Here, the beneficial effect of scaling down the size of the BFM to achieve higher bending angles is noticeable, as demonstrated by several significant differences that were identified among the tested cases. In particular, BFM-B was more effective than the BFM-A in reaching higher bending angles when stimulated at 0.66 and 1 V mm^{-1}.

It is noteworthy to mention that displacement was not influenced by the variation of the pulse width (2, 4, and 10 ms), which minimally contributed to increasing the performance of such a mechanism even when applying higher electrical fields (Figure S3, Supporting Information). These results highlight that

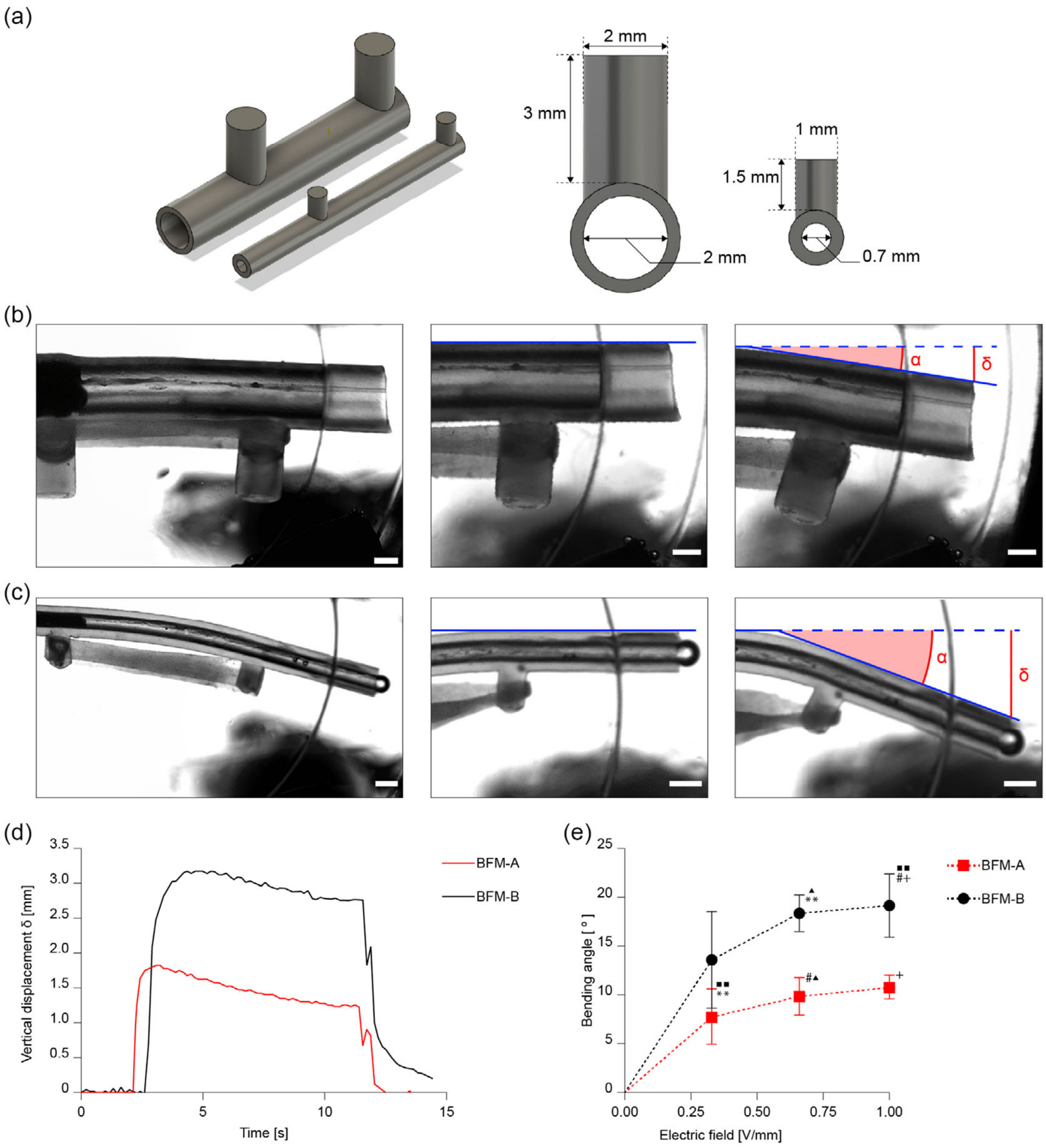

Figure 3. Comparison of actuation performance in biohybrid flexure mechanisms of different sizes. a) Structural comparison of the biohybrid flexure mechanism A (BFM-A) and biohybrid flexure mechanism B (BFM-B) in terms of size of the components. b) Images of the BFM-A in its entirety (left image), prior to applying Electrical Pulsed Stimulation (center image), and following the stimulation (right image). Scale bar: 2 mm. c) Images of the BFM-B in its entirety (left image), prior to applying electrical pulsed stimulation (center image), and following the stimulation (right image). Scale bar: 1 mm. d) Representative comparison of the vertical displacement overtime for the BFMs, applying an electrical field of 1 V mm^{-1} with a pulse width of 2 ms. e) Bending angle achieved by the BFMs according to the different electrical fields (0.33, 0.66 and 1 V mm^{-1}, pulse width: 2 ms) applied to the bioactuator. Data are reported as mean and standard deviation. Statistical differences were analyzed by two-way ANOVA, and defined with different symbols ($-p$ value < 0.05, $+ = p$ value < 0.05, $\# = p$ value < 0.05, ■■ $= p$ value < 0.01, $** = p$ value < 0.01). $N = 3$.

the intensity of the electric field is the most critical parameter to control the bending angle and the vertical displacement. Indeed, the deformation of the monolithic flexible substrate was mainly regulated by the magnitude of the electrical stimulation, which increased the contractile response of the bioengineered skeletal muscle tissue. It is worth mentioning that this configuration takes advantage of a lower local buckling resistance induced by the relatively low ratio between the wall thickness and the external diameter of the skeleton. Also, the blend of silicone used in this study is relatively soft (Young's modulus: 0.11 MPa) compared to other reported systems,[9,12–15,17,19] and this led us to increase the performance of the BFM with respect to the state of the art. Indeed, the deflection values in terms of bending angle or vertical displacement found with this novel design currently outperform what is the state of the art of biohybrid robots.[11,44] For example, Guix et al. reported a maximum displacement of ≈100–200 µm s^{-1} in the best-performing system, which is an order of magnitude lower than the values observed in the present study.[19] Additionally, the force generated by the muscle actuator was around 150 μN, also lower than the values measured here. The serpentine-like structures employed in that work enabled deformation through low geometrical stiffness and incorporated a restoring force to return the bio-bot to its original position. However, that configuration, in terms of both geometry and material properties, did not allow for the simultaneous maximization of displacement and force output. In another study, Wang et al. demonstrated that a single-muscle-strip bio-bot was capable of generating an active force of up to 1.5 mN.[18] Nevertheless, the overall displacement of the system was constrained by the stiffness of the supporting pillars, which limited deflection during muscle contraction to less than 150 μm, thereby limiting also the locomotion capability of the bio-bot.

Evaluating the cyclic actuation of biohybrid machines is essential to assess their functional stability, durability, and reliability overtime, especially for applications requiring repeated and sustained performance. The performance of the BFM-A and BFM-B over cyclic actuation was also evaluated to assess whether the performance of these mechanisms would decrease overtime as a result of repeated tetanic stimulation at 30 Hz. For this purpose, an asymmetric waveform at 1 V mm^{-1} with a 4 ms pulse width was applied to determine the contraction of each BFM over six 5 s ON/OFF cycles (**Figure 4**a).

Results showed that in the case of BFM-A, the average bending angle varied from 5.52° ± 2.83° to 5.84° ± 2.83° (Figure 4b). In contrast, the average bending angle for BFM-B varied from 12.21° ± 2.40° to 9.6° ± 2.08° (Figure 4c). Movie S3 and S4, Supporting Information, show the different deflections achieved for BFM-A and BFM-B upon the cyclic application of electrical stimulation at 1 V mm^{-1}. The bending angle achieved upon electrical stimulation did not change significantly over this period, meaning that the application of such tetanic stimulation did not interfere with muscle functionality.

These results also demonstrated that flexural rigidity plays a relevant role in designing a BFM for maximizing functionalities in biohybrid soft robotics. Flexural rigidity is a constant property determined by the material and cross-sectional area, and this concept is essential for understanding the overall stiffness of structures. Flexural rigidity denotes the mechanical resistance of a structure subjected to a load while undergoing bending. Therefore, low flexural stiffness is more advantageous for maximizing the flexure mechanism deflection. Such value depends on both the material properties (such as Young's modulus) and the geometry of the cross-sectional area (such as the second moment of area, or moment of inertia). For structures like the BFM (hollow tubular structure), the moment of inertia can be defined as follows:

$$I_0 = \frac{\pi(D^4 - d^4)}{64} \quad (1)$$

where D is the outer diameter and d is the internal diameter. The flexural rigidity of a material can be synthesized with the following equation:

$$Fl = E \cdot I_0 \quad (2)$$

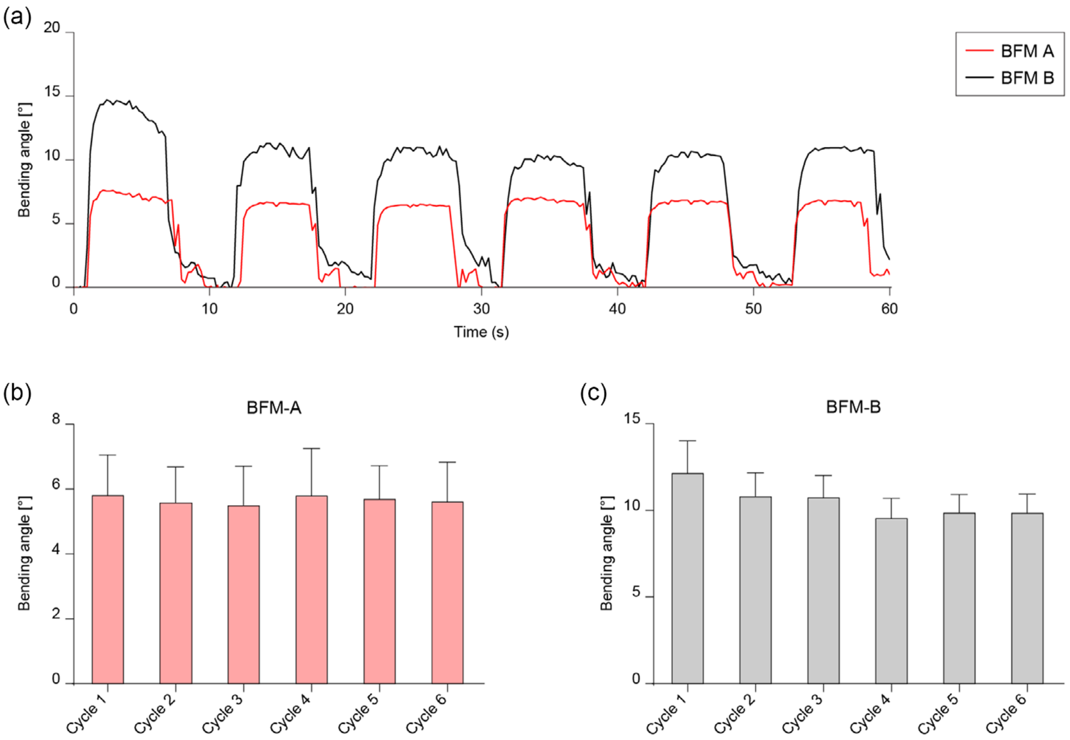

Figure 4. Comparison of actuation performance in biohybrid flexure mechanisms of different sizes undergoing cyclic actuation. a) Comparison of the average bending angle achieved by the BFMs stimulated at 1 V mm^{-1} over six 5 s ON/OFF cycles. b) Comparison of the average bending angle achieved at each stimulation cycle for BFM-A. c) Comparison of the average bending angle achieved at each stimulation cycle for BFM-B. Data are reported as mean and standard deviation. Statistical differences were analyzed by two-way ANOVA. $N = 5$.

where E is the Young's modulus of the material used. This equation indicates that flexural rigidity depends on the material stiffness (E) and the shape and size of the cross-sectional area (I_0), but not on the external load. Indeed, a structure with lower internal and external diameters may show a decreased resistance to the torque exerted by the contraction of the biohybrid actuator. We investigated the performance of a structure analyzing a difference of one order of magnitude as the difference in the flexural rigidity of the BFM decreased from a value of 0.16 Nmm^2 (internal diameter: 2 mm) to a value of 0.014 Nmm^2 (internal diameter: 0.7 mm).

Unlike traditional rigid hinges, the monolithic BFM using bioengineered muscle tissue offers several advantages. These include the reduction of manufacturing complexity, as monolithic structures are created in a single process from a single piece of material and could simplify designs, reducing the need for bulky or complex mechanical parts and susceptibility to wear, friction, and mechanical failure,[20,21] and the reduction in size and weight, as these configurations can be made more compact and lightweight. The inherent simplicity of monolithic designs allows for easy scaling in both microscale and macroscale applications, that is highly functional in fields like biohybrid actuators, where scalability is key for adapting to different applications.

Monolithic structures allow for efficient transfer of forces generated by bioengineered muscle tissues, minimizing the energy losses associated with joints or other assembled parts. This results in smoother, more predictable actuation, maximizing the power output from muscle contractions. Indeed, the BFM allows for smooth and adaptable movements that may resemble natural muscle motion, without the rigidity seen in traditional mechanical systems. In contrast with Takeuchi et al. who investigated a thin parylene skeleton to build hinges in biohybrid robots,[11,20,28,45] soft silicones represent candidate materials for applications requiring natural and smoother motion and the recovery of the initial position after bending without permanent deformation or tearing. Flexure joints in biohybrid robots must operate in the elastic region of the material, and the flexibility of silicone, together with the monolithic configuration, allows for the muscle tissue to generate smoother bending motions, akin to biological systems, avoiding potential issues due to friction or tearing. The stiffer nature of parylene might limit the degree of curvature and lead to more discrete, steplike motions rather than the smooth, adaptable, and continuous flexing noticeable in silicone-based substrates. Furthermore, the high elasticity of silicone allows it to withstand greater deformation without experiencing mechanical fatigue or damage, which is also one of the major drawbacks of several flexure-based mechanisms.[23]

The hollow cylindrical configuration of the BFM can provide the stage for a structure that may resist bending compared to other configurations, like thin films, due to the inherent geometric properties of tubular shapes, which distribute stresses more evenly and provide better structural stability. The BFM represents a lightweight and flexible structure due to the control of the geometrical parameters like internal and external diameters. Nevertheless, such a configuration may enable other functionalities thanks to its structural conformations, for example, drug delivery or endoscopy.[46] **Figure 5** shows two examples of possible applications of the BFM to better highlight the potential of this architectural design.

In the first demonstrator, the BFM was used to selectively release a model drug (represented by a fluorescent dye, e.g.,

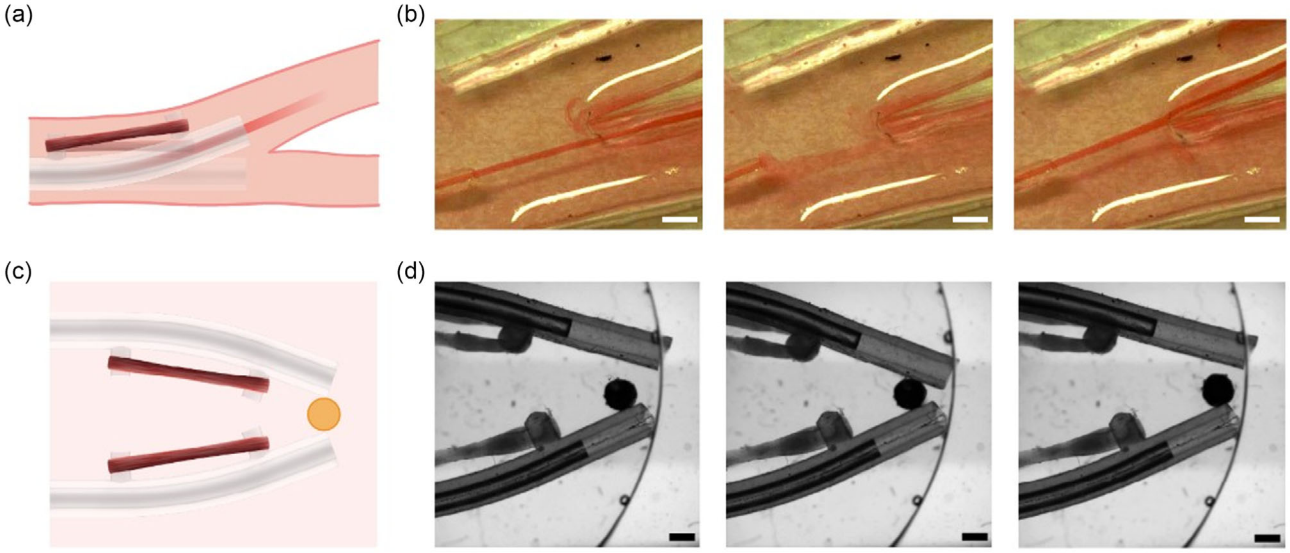

Figure 5. Overview of two proof of concepts investigated for the proposed biohybrid flexure mechanism. a) Artistic illustration of the biohybrid flexure mechanism (BFM) used to guide the release of substances at a vessel bifurcation, for targeted therapy. b) Depiction of the directional release of a colored dye through a syringe pump thanks to the actuation of the muscle actuator. First, the BFM (BFM-B in this specific example) can release the substance into a vessel (left). Then, the stimulation of the muscle tissue enables the deflection of the BFM (middle) to direct the release of the substance toward a second vessel (right). Scale bar: 2 mm. c) Artistic illustration of a gripper based on the use of two BFMs to grip a spherical particle (size: ≈500 μm). d) Depiction of the sequential phases of gripping using two BFMs-B. In the first phase (left), muscle actuators were relaxed. Subsequently (middle), both muscle tissues were activated, and their contraction favored the stable gripping of the particle. Finally, both muscle actuators were relaxed by ceasing the electrical stimulation. Scale bar: 1 mm.

red) into a targeted vessel at a bifurcation point (Figure 5a). This was achieved through the specific configuration of the BFM, which featured a hollow channel that could be directionally bent upon muscle stimulation (Figure 5b, Movie S5, Supporting Information). The contraction of the muscle tissue transmitted force through pillars, enabling a controlled flexural movement and precise directional release. Indeed, the hollow conformation of the BFM may enable drug release through its conduit.[47]

In the second demonstrator, two BFMs constituted a soft robotic gripper able to grasp a small spherical polystyrene particle (≈500 μm in diameter) (Figure 5c). Upon contraction of the muscle tissue, the BFMs bent inward, gripping the target object (Figure 5d, Movie S6, Supporting Information).

These demonstrators support the potential impact of BFM-targeted applications in the field of biohybrids, especially in contexts such as localized therapies within biohybrid-compatible environments (e.g., the human body) and the manipulation or gripping of milli- and microscale objects.

2.4. FE Simulations to Estimate the Force Exerted to Actuate the BFM

FE simulations were used to estimate the force exerted by the bioengineered skeletal muscle tissue for each condition. **Figure 6**a shows the simulation scenario used to find the force exerted by the bioactuator. The force was derived from a displacement-controlled simulation applied on the Y axis, in which the displacement resulting in the Z axis (U_z) was compared to that obtained in the experimental measurements (namely the vertical displacement mentioned in Section 2.3).

The displacement U_z of the BFM-A (Movie S7) and BFM-B (Movie S8) stimulated at 1 V mm^{-1} was successfully reproduced, with an error of less than 5% with respect to the experimental results (Figure 6b). Simulations facilitate comprehension of the forces exerted by the bioactuator in both mechanisms during the contraction phase. In fact, the force needed to achieve those vertical displacements resulted in 1.59 mN for the BFM-A and 0.37 mN for the BFM-B. These values are lower than the results reported in Figure 1c, which can be considered as the maximum force threshold that can be exerted by the 3D bioengineered skeletal muscle. Indeed, natural muscles are featured by a tension–length relationship,[48,49] which indicates a nonlinear relationship between the force exerted and their contraction/extension. In the experimental results, we dealt with the flexural rigidity of the mechanisms, the deformation of the pillars, and the force generated by the actuator according to its strain (active tension from contraction). While the influence of the pillars in terms of stiffness was negligible due to the intrinsic homogeneous composition of the monolithic BFM (data not shown), we found that the vertical displacement increases as the flexural rigidity decreases, leading to a reduction in the force experienced by the mechanism. It is noticeable to remark that the strain of the muscle ring was 5.2% and 6.6% for the BFM-A and BFM-B, respectively. Thus, the smaller mechanism (BFM-B) experienced a lower contraction force and a higher strain from the bioactuator, as it opposed a lower mechanical resistance to the contraction of the bioengineered muscle tissue (Figure S4, Supporting Information). Likely, the limited strain of the bioactuator was the limiting factor rather than the force. Such strain values are also comparable with what can be found in literature for bioengineered skeletal muscle tissues. Indeed, we found strains up to 6.6% of the initial length, while recent works amounted to values lower than 5% in the case of soft flexures,[31] and even lower (1%–4%) when compared with contractile C2C12-derived muscle during exercise.[12,13] Thus, we also demonstrated that the strain of the bioengineered skeletal muscle can be increased by utilizing the BFM.

In vitro bioengineered muscle tissues are limited in the force exerted and in the strain, making this kind of actuation mechanism intrinsically limited in terms of performance. Nonetheless, playing with the material properties and geometric design of the BFM, we achieved a relevant deformation of the mechanism with values of displacement that outperform those actually present in literature. These results support the fact that these designs would be suitable for building BFMs, and that there is broad margin to optimize their design, maximizing their vertical displacement and bending angle.[1] In fact, monolithic designs can be further engineered by altering their morphology to flex or deform in specific, predictable ways in response to muscle contraction,[50,51] and integrated in multi-degrees-of-freedom systems, enabling advanced functions in the field of biohybrid soft robotics.

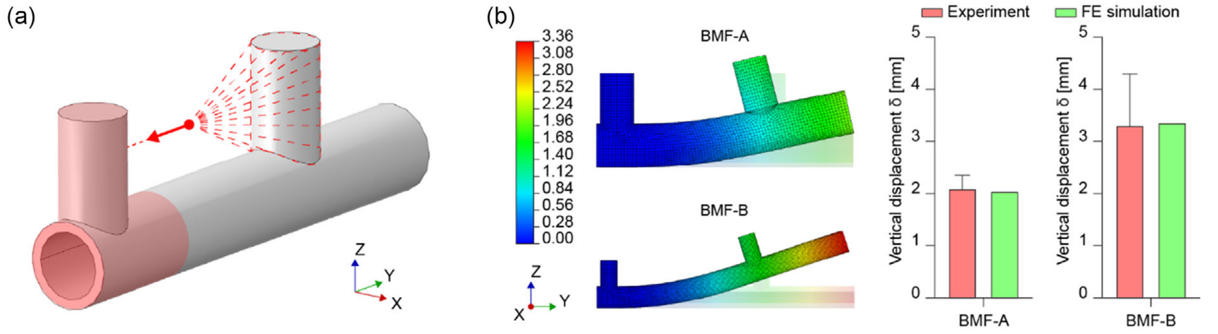

Figure 6. Biohybrid flexure mechanism modeling through finite-element simulations. a) Representative image of the simulation environment for the biohybrid flexure mechanism (BFM) analyzed in this study. The red-colored part of the BFM represents the area that was simulated as a fixed joint (*encastre*), replicating the same situation of the experimental in vitro test, while the red arrow represents the applied displacement that induced the deformation of the BFM. b) Images of the finite-element (FE) simulations outcomes, highlighting the different vertical displacements achieved by the two mechanisms, and graphs describing the differences between FE predictions (vertical displacement) and the experimental results.

3. Conclusion

In this work, we introduce a novel BFM actuated by a bioengineered skeletal muscle tissue, with potential use within the field of biohybrid soft robotics. We developed and characterized a specific design, based on a hollow tubular structure made of a soft, biocompatible silicone blend made of PDMS and Ecoflex, intended to minimize the flexural rigidity of the skeleton, thus maximizing the bending response upon muscle contraction.

Two distinct configurations were tested to evaluate the effect of flexural rigidity on the bending angles and vertical displacements of the proposed BFMs. Results highlight the critical role of geometric design and material selection in tuning the mechanical response of monolithic BFMs across different scales, paving the way to further possibilities of design optimization to maximize the performance, or deform the BFM in specific, predictable ways in response to muscle contraction. For this scope, the use of machine learning algorithms would facilitate the optimization process.[52]

In summary, the proposed BFM demonstrates promising versatility for applications where biocompatibility, soft actuation, flexibility, and control are important, making it a valuable addition to the toolkit of biohybrid soft robotics. Muscle-actuated systems could have impactful applications in soft robotics, or for the design of minimally invasive medical devices, such as steerable robotic instruments for diagnostics or therapeutic interventions, as catheters for targeted drug delivery or biopsy collection,[27,53] or endoscopes equipped with illumination for navigating complex anatomical pathways.[54]

4. Experimental Section

C2C12 Cell Culture and Biofabrication of 3D Skeletal Muscle Tissues: C2C12 mouse myoblasts (ATCC, CRL-1772) were cultured in T-175 flasks using GM composed of high-glucose Dulbecco's modified Eagle's medium (DMEM), supplemented with 10% fetal bovine serum (FBS), 200 nM l-glutamine, and 1% penicillin–streptomycin (all from Gibco). C2C12 cells were mixed at a concentration of 10 M mL^{-1} with a hydrogel matrix composed of 30% v/v Matrigel (Corning), 4 U mL^{-1} of thrombin (Sigma-Aldrich), 4 mg mL^{-1} of fibrinogen (Sigma-Aldrich), 16% v/v of GM supplemented with 1 mg mL^{-1} aminocaproic acid (ACA, Sigma-Aldrich). Then, 60 μL of the cell-laden mix was cast in a PDMS-based circular ring mold (3.6 mm internal radius and 5.1 external radius) that was previously 3D printed using a Cellink's Inkredible + 3D Bioprinter and cured at 65 °C overnight. The cell-laden hydrogel was cultured in GM with ACA for 2 days in an incubator at 37 °C and 5% CO_2 for 2 days, then transferred and assembled to a Petri dish containing a PDMS-based two-post system (3 × 2 × 0.3 mm) that was previously 3D printed and cured at 37 °C for 7 days. The 3D skeletal muscle tissue was maintained in the two-post system during the differentiation process (for at least 7 days), cultured in DM composed of DMEM supplemented with 10% horse serum (Gibco), 200 nM l-glutamine (Gibco), 1% penicillin–streptomycin (Gibco), Insulin-like growth factor 1 (IGF-1, 50 ng mL^{-1}; Sigma-Aldrich), and 1 mg mL^{-1} of ACA.

Actin Staining and Immunofluorescence Imaging of the 3D Skeletal Muscle Tissues: Muscle tissues were washed three times with PBS 1x before being fixed in 4% PFA for 1 h at room temperature (RT). Then, after PBS washings, the samples were permeabilized with 0.05% of Triton X-100 (Sigma Aldrich, X100) for 15 min at RT, washed again incubated with 5% BSA in PBS for 40 min at RT. After PBS washing, the samples were incubated for 2 h at RT and dark conditions with ActinRed 555 ReadyProbes Reagent following the manufacturer's guidance to stain the actin filaments of the muscle cells. Subsequently, samples were washed and incubated for 10 min with a 0.5 μL mL^{-1} Hoechst 33 342 solution in PBS (Invitrogen, H1399). Finally, a Leica Thunder microscope was used to image samples.

Force Measurements of the 3D Skeletal Muscle Tissues: A protocol reported in the literature was followed to evaluate the contractile behavior of the muscle tissues.[10] Briefly, muscle tissues assembled in the two-post systems (i.e., the same system where they were cultured during the differentiation process) were electrically stimulated by applying train of pulses of 10 and 30 s durations to induce twitch contractions at 1 Hz and tetanic contractions at 30 Hz, respectively. The stimulation consisted of asymmetric charge-balanced waveforms with an amplitude of 15 V (electric field: 1 V mm^{-1}), 4 ms pulse width, and 1 and 30 Hz frequency. Stimulation waveforms were generated using a custom MATLAB script using a ratio between the anodic and cathodic phases of 0.5.[55] The generated waveforms were then loaded into the arbitrary function generator Analog Discovery 2 (Digilent, USA). To obtain stimuli of the desired magnitude, the output of the function generator was then amplified using the bench amplifier Model 9200 (Tabor Electronics, Israel). The stimulation setup is shown in Figure S5, Supporting Information. Muscle contraction generates a force towards flexible posts, which bend synchronized with the electrical pulse applied. The post bending was recorded using the Leica Thunder microscope and the videos were analyzed using a custom-made Python code, which provided the displacement of the post overtime. Euler–Bernoulli's beam bending equation was used to correlate the bending of the post with the force exerted by the muscle tissue, that is, using the following equation:

$$P = \frac{3 \cdot E \cdot Iz \cdot y(a)}{a^3} \tag{3}$$

where P is the applied force, E is Young's modulus, Iz is the second moment of area of the post around the Z axis, a is the height from which the tissue is exerting the force, and $y(a)$ is the displacement of the post at this height. Contraction force values were normalized to the muscle tissue area, considering it as a cylindrical structure. The cross-sectional area was calculated (area $= \pi r^2$), where the radius (r) was measured using the ImageJ software.

Material Selection for the BFMs and Analysis of the Mechanical Properties: The material used to fabricate the BFMs derived from the analysis of a mixture of two components: PDMS (Sylgard 184 silicon elastomer kit, Dow Corning) and EcoFlex 00-10 (EcoFlex, Smooth-On). First, EcoFlex was poured into a beaker with components A and B, followed by the addition of PDMS (only monomer). The beaker was then placed in a SimplyMix Mixer (IGT) and kept for 60 s to homogeneously mix the two materials. The samples were then subjected to curing in an oven at 50 °C for 1 h and 30 min and left at RT for 2 h and 30 min. Different ratios were evaluated by varying the ratio between PDMS and EcoFlex, from 1:1 to 1:10.

Mechanical assessment of the different PDMS-EcoFlex formulations was performed by tensile tests through an Instron machine (model 5965, load cell: 1 kN, Instron, Norwood, MA, USA). The tensile speed applied was 10 mm min^{-1}. Materials were cast into molds made of resins fabricated with a 3D printer (HD3000, ProJet), conforming to ASTM D412-Type C standards, after the application of the Ease Release onto the molds to ease their detachment. The Young's modulus was derived from the slope of the first 10% of the stress–strain curve.

Assessment of the Material Biocompatibility: The biocompatibility of the material formulation selected to fabricate the BFM (PDMS-EcoFlex 00-10 ratio of 1:10) was evaluated by assessing the viability of murine skeletal muscle cells (ATCC, CRL-1772) when in contact with the supernatants derived from the incubation of a piece of material within culture medium (conditioned medium).

For this purpose, cylindrical molds (diameter: 13 mm; height: 3 mm) of the material selected, and those fabricated with PDMS 10:1, EcoFlex 00-10 were fabricated. The samples were disinfected by washing in a 70% v/v bath for 1 h, with rotation after 30 min to ensure both sides were treated. Following this, both sides were rinsed twice with 1x PBS for 5 min. Finally, the samples were exposed to UV light for 40 min per side. C2C12 cells at passage 6 were cultured in GM made of high glucose DMEM supplemented with 10% FBS v/v, 100 IU mL^{-1} penicillin, and 100 μg mL^{-1}

streptomycin. The material samples were incubated in a 24-well plate with GM for 24 h to produce a conditioned medium. After 24 h, the samples were removed, and the previously cultured cells were seeded at a density of 5000 cells cm^{-2} in a new 24-well plate with the conditioned medium for 72 h. On the third day, the following tests were conducted: analysis of the metabolic activity (PrestoBlue assay), the release of LDH, and the cell viability (Live/Dead assay). These assays were performed according to the manufacturer's instructions.

BFM Fabrication: The components of the mold were designed using the software Autodesk Fusion (Autodesk), and the various mold components were fabricated through stereolithography (Form 3B+, FormLabs), utilizing Surgical Guide Resin (FormLabs). As shown in Figure S1a, Supporting Information, the molds consisted of four elements and a metal plug matching the internal diameter of the BFM. The base included two concentric holes for positioning the plug and allowing material flow for the desired wall thickness, along with two holes for material injection and four for 6 cm screws to ensure axial alignment. Two lateral components fit around the plug, with semicircular cavities matching the catheter's external radius; one lateral piece has two additional holes for pillar fabrication. Both lateral parts have two holes for 6 cm screws and four smaller ones for 4 cm screws to secure them together. The upper piece resembles the base, with similar concentric holes, four for 6 cm screws, and two smaller holes to allow air escape during material injection. Two molds were prepared: one with a 2 mm internal diameter and 300 μm wall thickness (external diameter = 2.6 mm), and the other with a 0.7 mm internal diameter and 300 μm wall thickness (external diameter = 1.3 mm).

Molds were used to produce the BFMs in a monolithic configuration, according to the following steps. First, a release agent (Ease Release 200) was sprayed onto all mold components to aid in the release of the silicone. The components were left to dry for at least 10 min. After the material was mixed, it was poured into two syringes (volume: 6 mL) and placed in a degasser for at least 10 min to remove any air bubbles. Once degassed, the material was ready to be injected into the mold to fabricate the prototype.

Then, the mold components were assembled, except for the lateral piece containing the holes for the pillars. The material was initially injected into the holes for the pillars, and once the mold was completely assembled, it was injected through the base holes to ensure the entire mold was filled. The mold was then placed in an oven at 50 °C for 1 h and 30 min, followed by an additional 24 h at RT before being opened.

Analysis of the BFM Motion: Analysis was conducted using a specialized setup that allowed for various stimulation configurations by combining different voltages and pulse widths. The setup consisted of a waveform generator and an amplifier, connected to two electrodes positioned inside a Petri dish (diameter: 60 mm). Once the setup was prepared, real-time imaging was performed with the Leica Thunder microscope for each sample to capture the muscle contraction.

The vertical displacement and the bending angle were measured using a custom-made Python script capable of identifying the flexure mechanism and its tracking points (P1, P2, and P3) to subsequently calculate $\propto$ and δ after video analysis (Figure S6, Supporting Information). For each frame, the script determined $\propto_t = \arctan(\overline{p2_t p3_t}/\overline{p1_t p3_t})$ and $\delta_t = |p2_t p3_t|$were computed for each video frame. The maximum values across the entire video were then calculated as

$$\propto = \max_{t=1,2,\ldots,N}(\propto_{t-t_0} - \propto_{t-t_0}) \text{ and } \delta = \max_{t=1,2,\ldots,N}(\delta_{t-t_0} - \delta_{t-t_0}) \tag{4}$$

Where N Represents the Video Frames: The stimulation was performed applying a train of 10 s of biphasic asymmetric charge balanced stimuli with amplitude of 5, 10, and 15 V, frequency of 30 Hz and pulse widths of 2, 4, and 10 ms. The recorded videos were analyzed to measure the mechanisms bending. Three different skeletal muscle tissues for each design were tested.

Cyclic actuation was evaluated at day 10 of skeletal muscle differentiation using the flexure mechanisms of both sizes. Five skeletal muscle tissues were electrically stimulated using an asymmetric waveform at 15 V, 30 Hz, with a 4 ms pulse width, over six 5 s ON/OFF cycles. The actuation was recorded using the Leica Thunder microscope. Videos were analyzed to measure the mechanisms bending, as previously mentioned.

FE Simulations: The actuation of the two configurations of BFM was analyzed through FE analysis by means of the commercial software Abaqus 2020 (Dassault Systems).

A displacement-oriented approach was pursued to determine a displacement in the Z axis (Uz) comparable with what was experimentally obtained. At this purpose, a displacement was applied to a reference point located equidistant between the centroids of the circular cross sections of the two pillars along the Y axis, positioned at a height corresponding to half the pillar height, in which the bioengineered muscle tissue was placed. The displacement in the Y axis was iterated to approach the displacement in the Z axis (Uz) measured experimentally and was set to 0.65 mm for the BFM-A, and to 0.48 mm for the BFM-B. A fixed joint (*encastre*) was applied to the first pillar to block its deformation and simulate the experimental conditions provided by the support pin (as reported in Figure 1a). The PDMS-EcoFlex blend was modeled as a hyperelastic material, with the stress–strain experimental curve used as input in Abaqus. This data was fitted to an Ogden model, yielding parameters of $\alpha = 2.58$, $\mu = 2.83$, $D = 0$, and $N = 1$ (Figure S7, Supporting Information). The choice of the Ogden model for this material is based on the approach proposed by Steck et al.[56] These parameters define the Ogden model's strain energy function (W) as follows:

$$W = \sum_{i}^{N} \frac{2\mu_i}{\alpha_i^2}(\lambda_1^{-\alpha i} + \lambda_2^{-\alpha i} + \lambda_3^{-\alpha i} - 3) + \sum_{i}^{N} \frac{1}{D_i}(J-1)^{2i} \tag{5}$$

where λ are the principal stretches and N, α, and μ are the model constants. The chosen procedure for the model was "Static, general".

Statistical Analysis: A normality test (Shapiro-Wilk) was performed on all experimental data to assess data distribution. Then, the data were analyzed based on their type of distribution, as described in the figure captions. Statistical analyses were carried out using GraphPad Prism (v 9). The significance threshold was set at 5%.

Supporting Information

Supporting Information is available from the Wiley Online Library or from the author.

Acknowledgements

This project has received funding from the European Union's Horizon Europe research and innovation program under grant agreement no. 101070328 (BioMeld project). The authors acknowledge the support of the BRIEF "Biorobotics Research and Innovation Engineering Facilities" (project identification code IR0000036), project funded under the National Recovery and Resilience Plan (NRRP), Mission 4 Component 2 Investment 3.1 of Italian Ministry of University and Research funded by the European Union—NextGenerationEU, and the CERCA program by the Generalitat de Catalunya, the Secretaria d'Universitats i Recerca del Departament d'Empresa i Coneixement de la Generalitat de Catalunya, and the "Centro de Excelencia Severo Ochoa" (grant no. CEX2023-001282-S, funded by MICIU/AEI/10.13039/501100011033).

Open access publishing facilitated by Scuola Superiore Sant'Anna, as part of the Wiley - CRUI-CARE agreement.

Conflict of Interest

The authors declare no conflict of interest.

Data Availability Statement

The data that support the findings of this study are available from the corresponding author upon reasonable request.

Keywords

bioactuator, biohybrid robotics, flexible skeleton, microfabrication, muscle contraction, muscle tissue engineering, soft robotics

Received: November 16, 2024
Revised: April 16, 2025
Published online: May 27, 2025

---

[1] L. Ricotti, B. Trimmer, A. W. Feinberg, R. Raman, K. K. Parker, R. Bashir, M. Sitti, S. Martel, P. Dario, A. Menciassi, *Sci. Robot.* **2017**, 10.1126/scirobotics.aaq0495.
[2] Y. Yang, Y. Wu, C. Li, X. Yang, W. Chen, *Adv. Intell. Syst.* **2020**, *4*, 1900161.
[3] O. Aydin, A. P. Passaro, R. Raman, S. E. Spellicy, R. P. Weinberg, R. D. Kamm, M. Sample, G. A. Truskey, J. Zartman, R. D. Dar, S. Palacios, J. Wang, J. Tordoff, N. Montserrat, R. Bashir, M. T. A. Saif, R. Weiss, *APL Bioeng.* **2022**, *6*, 010903.
[4] I. W. Hunter, S. Lafontaine, in *Technical Digest IEEE solid-state sensor and actuator workshop*, IEEE, Piscataway, NJ **1992**. pp. 178-185.
[5] D. R. Higueras-Ruiz, K. Nishikawa, H. Feigenbaum, M. Shafer, *Bioinspir. Biomim.* **2021**, *17*, 011001.
[6] S. P. Cairns, F. Borrani, *J. Physiol.* **2015**, *593*, 21.
[7] I. Venturino, V. Vurro, S. Bonfadini, M. Moschetta, S. Perotto, V. Sesti, L. Criante, C. Bertarelli, G. Lanzani, *Commun. Biol.* **2023**, *6*, 1148.
[8] L. Ricotti, T. Fujie, *Bioinspir. Biomim.* **2017**, *12*, 2.
[9] A. Hasebe, Y. Suematsu, S. Takeoka, T. Mazzocchi, L. Vannozzi, L. Ricotti, T. Fujie, *ACS Biomater. Sci. Eng.* **2019**, *5*, 11.
[10] R. Mestre, T. Patiño, X. Barceló, S. Anand, A. Pérez-Jiménez, S. Sánchez, *Adv. Mater. Technol.* **2019**, *4*, 2.
[11] K. Morita, Y. Morimoto, S. Takeuchi, *Biofabrication* **2023**, *15*, 4.
[12] C. Cvetkovic, R. Raman, V. Chan, B. J. Williams, M. Tolish, P. Bajaj, M. S. Sakar, H. H. Asada, M. T. A. Saif, R. Bashir, *Proc. Natl. Acad. Sci* **2014**, *111*, 28.
[13] R. Raman, C. Cvetkovic, S. G. M. Uzel, R. J. Platt, P. Sengupta, R. D. Kamm, R. Bashir, *Proc. Natl. Acad. Sci* **2016**, *113*, 13.
[14] R. Mestre, J. Fuentes, L. Lefaix, J. Wang, M. Guix, G. Murillo, R. Bashir, S. Sánchez, *Adv. Mater. Technol.* **2023**, *8*, 2.
[15] K. Kabumoto, T. Hoshino, Y. Akiyama, K. Morishima, *Tissue Eng. Part A* **2013**, *19*, 15.
[16] Z. Li, Y. Seo, O. Aydin, M. Elhebeary, R. D. Kamm, H. Kong, M. T. A. Saif, *Proc. Natl. Acad. Sci* **2019**, *116*, 5.
[17] G. J. Pagan-Diaz, X. Zhang, L. Grant, Y. Kim, O. Aydin, C. Cvetkovic, E. Ko, E. Solomon, J. Hollis, H. Kong, T. Saif, M. Gazzola, R. Bashir, *Adv. Funct. Mater.* **2018**, *28*, 23.
[18] J. Wang, Y. Wang, Y. Kim, T. Yu, R. Bashir, *APL Bioeng.* **2022**, *6*, 3.
[19] M. Guix, R. Mestre, T. Patiño, M. De Corato, J. Fuentes, G. Zarpellon, S. Sanchez, *Sci. Rob.* **2021**, *6*, 53.
[20] Y. Morimoto, H. Onoe, S. Takeuchi, *Sci. Rob.* **2018**, *3*, 18.
[21] R. Kinjo, Y. Morimoto, B. Jo, S. Takeuchi, *Matter* **2024**, *7*, 3.
[22] F. Cosandier, S. Henein, M. Richard, L. Rubbert, *The Art Of Flexure Mechanism Design*, Epfl Press, Lausanne **2017**.
[23] H. Chun, X. Guo, J. S. Kim, C. B. Lee, *Int. J. Adv. Manuf. Technol.* **2020**, *110*, 681.
[24] N. A. Yaraghi, D. Kisailus, *Annu. Rev. Phys. Chem.* **2018**, *69*, 23.
[25] T. Nomura, M. Takeuchi, E. Kim, Q. Huang, Y. Hasegawa, T. Fukuda, *Micromachines* **2021**, *12*, 4.
[26] Y. Akiyama, S. J. Park, S. Takayama, *Nanotechnol. Microfluid.* **2020**, 347.
[27] C. Salvatori, D. Trucco, I. Niosi, L. Ricotti, L. Vannozzi, in *Conference on Biomimetic and Biohybrid Systems*, Springer Nature, Switzerland **2023**. pp. 378–393.
[28] Y. Morimoto, H. Onoe, S. Takeuchi, *Adv. Robot.* **2019**, *33*, 5.
[29] L. Gao, M. U. Akhtar, F. Yang, S. Ahmad, J. He, Q. Lian, W. Cheng, J. Zhang, D. Li, *Acta Biomater.* **2021**, *121*, 29.
[30] F. Iberite, M. Piazzoni, D. Guarnera, F. Iacoponi, S. Locarno, L. Vannozzi, G. Bolchi, F. Boselli, I. Gerges, C. Lenardi, L. Ricotti, *ACS Appl. Bio Mater.* **2023**, *6*, 7.
[31] R. Raman, *Annu. Rev. Biomed. Eng.* **2024**, *26*, 223.
[32] N. Lynch, N. Castro, T. Sheehan, L. Rosado, B. Rios, M. Culpepper, R. Raman, *Adv. Intell. Syst.* **2024**, *6*, 2300834.
[33] R. Mestre, N. García, T. Patiño, M. Guix, J. Fuentes, M. Valerio-Santiago, N. Almiñana, S. Sánchez, *Biofabrication* **2021**, *13*, 4.
[34] B. G. Molina, J. Fuentes, C. Alemán, S. Sánchez. *Biosens. Bioelectron.* **2024**, *251*, 116117.
[35] S. Lai, J. Fuentes, M. Guix, G. Casula, P. Cosseddu, S. Sánchez, *Adv. Intell. Syst.* **2024**, 2400407.
[36] S. Someck, A. Levi, H. E. Sloin, L. Spivak, R. Gattegno, E. Stark, *Commun Biol.* **2023**, *6*, 950.
[37] D. R. Merrill, M. Bikson, J. G. Jefferys, *J. Neurosci. Methods.* **2005**, *141*, 2.
[38] I. Miranda, A. Souza, P. Sousa, J. Ribeiro, E. M. S. Castanheira, R. Lima, G. Minas, *J. Funct. Biomater.* **2021**, *13*, 2.
[39] Z. Liao, M. Hossain, X. Yao, R. Navaratne, G. Chagnon, *Polym. Test.*, **2020**, *86*, 106478.
[40] S. Park, K. Mondal, *ACS Appl. Mater. Interfaces* **2018**, *10*, 13.
[41] J. Vaicekauskaite, P. Mazurek, S. Vudayagiri, A. L. Skov, *J. Mater. Chem. C* **2020**, *8*, 4.
[42] S. Kim, J. Kang, I. Lee, J. Jang, C. B. Park, W. Lee, B. S. Bae, *Npj Flex. Electron.* **2023**, *7*, 33.
[43] Y. L. Yap, S. L. Sing, W. Y. Yeong, *Rapid Prototyping J.* **2020**, *26*, 8.
[44] Y. Kim, Y. Yang, X. Zhang, Z. Li, A. Vázquez-Guardado, I. Park, J. Wang, A. I. Efimov, Z. Dou, Y. Wang, J. Park, H. Luan, X. Ni, Y. S. Kim, J. Baek, J. J. Park, Z. Xie, H. Zhao, M. Gazzola, J. A. Rogers, R. Bashir, *Sci. Rob.* **2023**, *8*, 74.
[45] Y. Morimoto, H. Onoe, S. Takeuchi, *APL Bioeng.* **2020**, *4*, 2.
[46] L. Sun, Y. Yu, Z. Chen, F. Bian, F. Ye, L. Sun, Y. Zhao, *Chem. Soc. Rev.* **2020**, *49*, 12.
[47] B. Yang, W. Qian, L. Zhang, *Langmuir* **2024**, *40*, 22736.
[48] W. O. Fenn, W. B. Latchford, *J. Physiol.* **1933**, *80*, 2.
[49] H. E. Ter Keurs, T. Iwazumi, G. H. Pollack, *J. Gen. Physiol.* **1978**, *72*, 4.
[50] L. Vannozzi, T. Mazzocchi, A. Hasebe, S. Takeoka, T. Fujie, L. Ricotti, *Adv. Biosyst.* **2020**, *4*, 8.
[51] L. Vannozzi, L. Ricotti, M. Cianchetti, C. Bearzi, C. Gargioli, R. Rizzi, P. Dario, A. Menciassi, *Bioinspiration Biomimetics* **2015**, *10*, 5.
[52] M. A. Tsompanas, I. Balaz, *Front. Robot. AI* **2024**, *11*, 1337722.
[53] X. Hu, A. Chen, Y. Luo, C. Zhang, E. Zhang, *Comput. Assist. Surg.* **2018**, *23*, 21.
[54] C. F. Guimarães, R. Ahmed, A. Mataji-Kojouri, F. Soto, J. Wang, S. Liu, T. Stoyanova, A. P. Marques, R. L. Reis, U. Demirci, *Adv. Mater.* **2021**, *33*, 52.
[55] R. Collu, E. J. Earley, M. Barbaro, M. Ortiz-Catalan, *Sci Rep.* **2023**, *13*, 1588.
[56] D. Steck, J. Qu, S. B. Kordmahale, D. Tscharnuter, A. Muliana, J. Kameoka, *J. Appl. Polym. Sci.* **2019**, *136*, 5.